

Non-adiabatic corrections to a chiral anomaly in topological nodal semimetals

Matej Badin ^{1,2,*}

¹SISSA – Scuola Internazionale Superiore di Studi Avanzati, Via Bonomea 265, 34136 Trieste, Italy

²Department of Experimental Physics, Faculty of Mathematics, Physics and Informatics,
Comenius University in Bratislava, Mlynská Dolina F2, 842 48 Bratislava, Slovakia

(Dated: January 27, 2022)

Studying many-body versions of Landau-Zener-like problem of non-interacting yet entangled electrons for several $\mathbf{k} \cdot \mathbf{p}$ models representing Weyl and Dirac semimetals, we systematically include non-adiabatic corrections to the quantum limit of the interband channel of conductivity connected to the chiral anomaly. Our study shows that a *relative homotopy invariant* [Sun, X. et al., Phys. Rev. Lett. **121**, 106402 (2018)] and *Euler class invariant* [Bouhon, A. et al., Nat. Phys. **16**, 1137–1143 (2020)] manifest in this conductivity channel. Moreover, we show that for *non-symmorphic systems* this contribution is sensitive to the direction of the applied magnetic field which suggests that the conjectured direction-selective chiral anomaly in non-symmorphic systems [Bzdušek, T. et al., Nature **538**, 75–78 (2016)] could lead to a strongly anisotropic longitudinal magnetoresistance. The presented approach can be easily applied to other $\mathbf{k} \cdot \mathbf{p}$ or tight-binding models.

I. INTRODUCTION

The characteristic feature of Weyl semimetals [1, 2] is the chiral anomaly [3, 4], experimentally manifested by a decrease of resistance in the presence of parallel electric and magnetic fields [5–12]. In the quantum limit of strong magnetic fields, the chiral anomaly of Weyl semimetals follows from the presence of chiral Landau levels (LLs) which connect the conduction bands to the valence bands. A pair of counter-propagating chiral Landau levels also appear in Dirac semimetals [1], where a similar signature in magnetoresistance is expected if the relaxation time of electrons is sufficiently large. Curiously, it has been reported that certain class of nodal-ring semimetals in non-symmorphic systems [13] should also exhibit chiral Landau levels, but only for special high-symmetry directions of the applied magnetic field.

In a Weyl semimetal, in the adiabatic limit, the motion of electrons can be modeled by the semi-classical approach [5–7], where the presence of chiral LL implies pumping of electrons from occupied to unoccupied bands at rate [5–7]

$$\frac{\partial Q}{\partial t} = -V \frac{e^3}{4\pi^2 \hbar^2} \mathbf{E} \cdot \mathbf{B}, \quad (1)$$

where V is the volume of the sample, \mathbf{E} is the electric field and \mathbf{B} is the magnetic field. This creation of conduction electrons corresponds to the chiral anomaly of Weyl fermions. Assuming a relaxation time τ , an equilibrium imbalance of conduction electrons and hole appear, which for a single Weyl fermion produces field-dependent conductivity [7]

$$\sigma(B) = \frac{e^3}{2\pi^2 \hbar} B \tau. \quad (2)$$

Since the longitudinal conductivity increases with the applied magnetic field, it follows that the longitudinal magnetoresistance is negative [7].

A similar method is inapplicable in certain other species of Weyl or Dirac semimetals. For example, Ref. [13] discovered so-called *non-symmorphic nodal loops* and *nodal chains* which exhibit very anisotropic LLs possibly exhibiting a direction-selective chiral anomaly. However, this conjecture cannot be studied within the adiabatic approximation because of occasional as well as symmetry-protected degeneracies in the corresponding LLs spectrum. Therefore, a way able to incorporate non-adiabatic corrections into the calculation is sought. However, in reality, many different intraband and interband channels contribute to the overall conductivity of a material. Hence, we limit ourselves only into the study of a simpler problem of non-adiabatic contributions to the pumping rate given by Eq. (1) (or its analogues). This prevents us from an introduction of an empirically determined relaxation time. Rather, we focus purely on the investigation how does the choice of magnetic field and a model symmetry affect the pumping rate - Eq. (1) (also in the non-adiabatic limit).

We note that recently two other approaches appeared [14, 15] which address the problem of calculation of magnetoresistance and nonlinear Hall effect in Weyl semimetals differently from the Refs. [5–7]. Ref. [14] defines the velocity by the gradient of band energy and solves the classical corresponding equation of motion for simple Fermi surfaces using semiclassical Boltzmann equation. Ref. [15] predicts nonlinear Hall effect in Weyl semimetals with broken inversion symmetry using semiclassical equation of motion for wavepackets.

This article is organized as follows. In Sec. II we describe a simple numerical method that enables to include non-adiabatic corrections to the pumping rate in the non-interacting yet entangled electron limit. In Sec. III and Sec. IV results of the method are presented for several orientations of magnetic fields for simple models that do and do not possess the *relative homotopy invariant* [16] or *Euler class invariant* [17], respectively. Finally, in Sec. V numerical results are presented for the class of Dirac semimetals possessing so-called *non-symmorphic nodal loops* [13].

* mbadin@sissa.it

II. METHOD

We consider a simpler many-body version of Landau-Zener-like problem of non-interacting electrons in $\mathbf{k} \cdot \mathbf{p}$ models under the presence of magnetic and electric fields. The later implies that we allow electrons to tunnel to neighboring LLs bands. We set Fermi level to zero energy, $\varepsilon_F = 0$, and consider the time-evolution of Slater determinants of momentum-dependent Hamiltonian under the presence of electric field. We consider only Slater determinants of electron states in which all electrons share the same value of momentum k_z . We model the presence of the electric field semiclassically as

$$\partial_t k_z = -eE/\hbar, \quad (3)$$

meaning that the electrons move along the 1D bands opposite to the direction of \mathbf{E} . The semi-classical motion is immediately solved as $k_z(t) = -eEt/\hbar$. The presence of magnetic field is modelled by the standard Peierls substitution in the corresponding $\mathbf{k} \cdot \mathbf{p}$ model. The time evolution of the system is modelled in the quantum limit following the time-dependent Schrödinger equation (TDSE),

$$i\hbar\partial_t |\psi(k_z)\rangle = \mathcal{H}^{\text{many}}(k_z) |\psi(k_z)\rangle, \quad (4)$$

where $k_z(t) = -eEt/\hbar$ and $|\psi(k_z)\rangle$ is the many-electron wave function expressed in the basis of Slater determinants. The state $|\psi(k_z)\rangle$ is initially ($t \rightarrow -\infty$) set to the state in which all LLs corresponding to the valence bands are completely filled. Under the assumption of non-interacting electrons, the many-electron Hamiltonian $\mathcal{H}^{\text{many}}(k_z)$ takes the form

$$\mathcal{H}^{\text{many}}(k_z) = \mathcal{H}(k_z) \otimes \dots \otimes \mathcal{H}(k_z), \quad (5)$$

where $\mathcal{H}(k_z)$ is the considered (single-particle) $\mathbf{k} \cdot \mathbf{p}$ model. For the given model and the fields E and B we calculate the pumping rate as

$$\frac{\partial Q}{\partial t} = -\frac{N_{\text{ex}}(E, B)e^2 E}{\Delta k_z \hbar} N_{\text{deg}} = -N_{\text{ex}}(E, B) \frac{e^3 V}{4\pi^2 \hbar^2} EB, \quad (6)$$

where $N_{\text{ex}}(E, B)$ is the expectation value of number of electrons in conductive bands at time $t \rightarrow \infty$ allowing for deviations from the adiabatic limit, see Eq. (1), $N_{\text{deg}} = \phi/\phi_0 = BL_x L_y / (2\pi\hbar/e)$ is the degeneracy of LL, $\Delta k_z = 2\pi/L_z$ is the spacing of the available states in the k -representation, $V = L_x L_y L_z$ is the volume of the sample and L_x , L_y and L_z are linear dimensions of the sample.

The technical details of the effective implementation of the numerical method are presented in the App. A.

III. RELATIVE HOMOTOPY INVARIANT

A. Models

In the presence of a mirror symmetry $m_z : (x, y, z) \mapsto (x, y, -z)$, a pair of mirror-related Weyl points (WPs) carry opposite chirality. While it is generally expected that such WPs

pairwise annihilate at the symmetric plane upon collision, it has been reported [16] that a finer relative homotopy invariant may prevent their annihilation, enforcing instead their conversion into a nodal loop (NL). Such a scenario prominently arises for two-band models based on a pair of orbitals with different m_z eigenvalue [18], while a trivial annihilation occurs if the two orbitals have the same mirror eigenvalue.

We consider minimal $\mathbf{k} \cdot \mathbf{p}$ models belonging to both topological classes, assuming for simplicity an additional SO(2) symmetry around the mirror normal. For the trivial case with mirror operator $\hat{m}_z = \mathbb{1}$, we take

$$\mathcal{H}_A(\mathbf{k}) = \hbar v (k_x \sigma_x + k_y \sigma_y) + (m - \alpha k_z^2) \sigma_z, \quad (7)$$

which for $m/\alpha > 0$ exhibits a pair of WPs at $(0, 0, \pm\sqrt{m/\alpha})$ that annihilate for $m = 0$ at $\mathbf{k} = \mathbf{0}$. For the non-trivial case with mirror operator $\hat{m}_z = \sigma_z$, the minimal model must include higher-order terms. We specifically take

$$\mathcal{H}_B(\mathbf{k}) = \alpha k_z (k_x \sigma_x + k_y \sigma_y) + (\beta (k_x^2 + k_y^2 - k_z^2) + m) \sigma_z, \quad (8)$$

which [similar to $\mathcal{H}_A(\mathbf{k})$ for $m > 0$] exhibits a pair of WPs at $(0, 0, \pm\sqrt{m/\beta})$, that [as opposed to $\mathcal{H}_A(\mathbf{k})$] convert to a NL in $k_z = 0$ with radius $\kappa = \sqrt{-m/\beta}$ for $m/\beta < 0$. A two-band model similar to $\mathcal{H}_B(\mathbf{k})$ (but with twice the value of the relative homotopy invariant, and with a flipped sign of the $k_z^2 \sigma_z$ term) has been considered for ferromagnetic HgCr₂Se₄ [19]. The recent work [20] showed that the relative homotopy invariant of the band nodes in HgCr₂Se₄ is of a delicate topological character.

A slightly adjusted version of $\mathcal{H}_A(\mathbf{k})$ also governs the conversion of WPs into NL in ZrTe, where the parameter m is manipulated by strain [17]; here, the topological stability is enhanced by a $C_2\mathcal{T}$ -protected non-Abelian topological invariant [21].

LLs of the models are presented in Figs. 1 and 2. In the numerical calculation we set the values of $\hbar v = \alpha = 1$ for $\mathcal{H}_A(\mathbf{k})$ and $\alpha = \hbar^2 \beta = 1$ for $\mathcal{H}_B(\mathbf{k})$.

B. Pumping rate

In Fig. 3 we show the expectation value of excited electrons in the conductive bands - $N_{\text{ex}}(E, B)$ (or to be more precise - $N_{\text{ex}}(\tilde{E}, \tilde{B})$, where \tilde{E} and \tilde{B} are rescaled fluxes of electric and magnetic fields E and B (to be defined later), respectively) - modifying the interband contribution to the conductivity due to the presence of chiral anomaly.

While the model $\mathcal{H}_A(\mathbf{k})$ without the additional SO(2) symmetry around the mirror normal does not show any significant additional structure in $N_{\text{ex}}(\tilde{E}, \tilde{B})$, see Fig. 1(a), the model $\mathcal{H}_B(\mathbf{k})$ possessing nontrivial SO(2) symmetry shows an additional structure for the magnetic field oriented along z-axis (for $m < 0$), see the *stripes* at Fig. 3(b). This structure is caused by gap closing at specific values of \tilde{m} , e.g., $\tilde{m} = -1$, see Fig. 1. These periodic-in- \tilde{m} gap closings are related to the

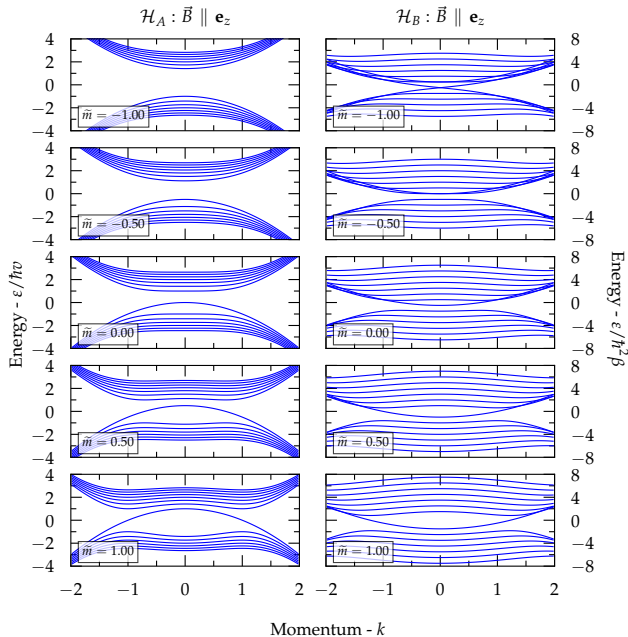


FIG. 1. LLs of $\mathcal{H}_A(\mathbf{k})$ and $\mathcal{H}_B(\mathbf{k})$ for the magnetic field oriented along the z-axis and $\tilde{B} = 0.5$ for various choices of \tilde{m} ($\tilde{m} = m/\hbar v$ for $\mathcal{H}_A(\mathbf{k})$ and $\tilde{m} = m/\hbar^2\beta$ for $\mathcal{H}_B(\mathbf{k})$). Note the pair of WPs for $\tilde{m} > 0$ for $\mathcal{H}_A(\mathbf{k})$ and the manifestation of the NL as a point in this orientation of magnetic field for $\mathcal{H}_B(\mathbf{k})$ and $\tilde{m} < 0$. Seven LLs below and above the Fermi level are shown.

gapless band structure of the nodal-loop phase, and are protected by mirror symmetry.

However, if one is given a WSM phase with two Weyl points that approach one another after tuning some parameter (e.g., \tilde{m}), then the \tilde{m} -dependence of the pumping rate in applied $\tilde{\mathbf{B}} \parallel \mathbf{e}_z$ does not reveal whether the Weyl points would annihilate or convert into the NL semimetal: we find that the dependence on the WSM side of the phase diagram (of $N_{\text{ex}}(\tilde{E}, \tilde{B})$) is qualitatively the same for both $\mathcal{H}_A(\mathbf{k})$ and $\mathcal{H}_B(\mathbf{k})$ (except the occasional gap closing at specific values of \tilde{m}).

But the models can be easily distinguished by the application of the magnetic field along the x-axis, where both models show the different structure of $N_{\text{ex}}(\tilde{E}, \tilde{B})$ in respect to the parameter \tilde{m} , see Fig. 3(c-d).

Namely, observe that the pumping rate for the Hamiltonian $\mathcal{H}_B(\mathbf{k})$ with non-trivial relative homotopy invariant is *de facto* constant as a function of \tilde{m} . In contrast, for $\mathcal{H}_A(\mathbf{k})$, where the Weyl points are able to annihilate, we observe a decrease in pumping rate *before* the Weyl points actually annihilate. This early vanishing of the chiral anomaly is particularly pronounced for small values of \tilde{E}/\tilde{B} (or E/B respectively; i.e., weak electric field, strong magnetic field.)

This can be easily explained by the occurrence of degenerate WP for $\mathcal{H}_A(\mathbf{k})$ while for $\mathcal{H}_B(\mathbf{k})$ NL or WP is always present in respect to \tilde{m} , see Fig. 2.

Furthermore, for sufficiently high values of \tilde{m} , $\mathcal{H}_A(\mathbf{k})$ and the magnetic field oriented along the z-axis, an interference

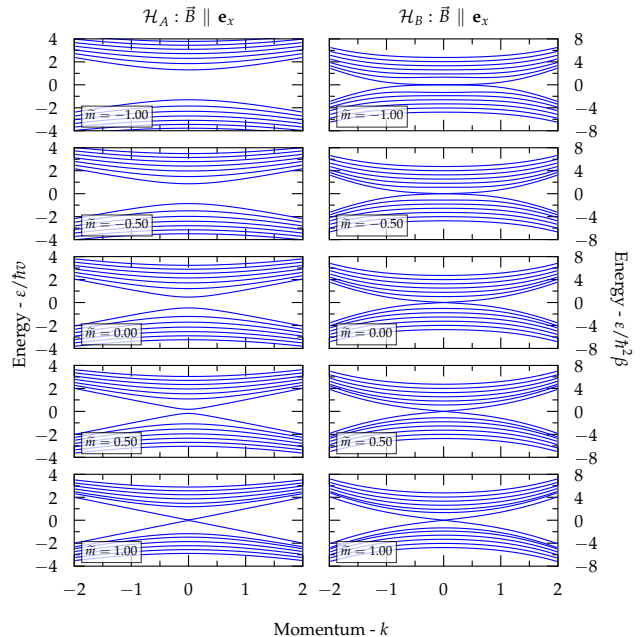


FIG. 2. LLs of $\mathcal{H}_A(\mathbf{k})$ and $\mathcal{H}_B(\mathbf{k})$ for the magnetic field oriented along the x-axis and $\tilde{B} = 0.5$ for various choices of \tilde{m} ($\tilde{m} = m/\hbar v$ for $\mathcal{H}_A(\mathbf{k})$ and $\tilde{m} = m/\hbar^2\beta$ for $\mathcal{H}_B(\mathbf{k})$). Note the NL for $\tilde{m} < 0$ and $\mathcal{H}_B(\mathbf{k})$. Seven LLs below and above the Fermi level are shown.

pattern can be observed on $N_{\text{ex}}(\tilde{E}, \tilde{B})$, see Fig. 3(a). It corresponds to the presence of top-most valence band close to the conduction bands at $k = 0$, see Fig. 1 - region around $\tilde{m} = 1$, where the sufficiently high value of \tilde{E} . The precise value of \tilde{m} for such a constructive/destructive interference to happen is determined by the time the electron in the top-most valence band spends in a vicinity of the conduction bands.

IV. EULER CLASS INVARIANT

A. Models

It is known that $C_{2z}\mathcal{T}$ symmetry (composition of time reversal with π rotation around the z axis) can stabilize Weyl points inside a symmetric plane $k_z = 0$ (or $k_z = \pi$), as observed e.g. in the $k_z = 0$ plane of WTe_2 [22], MoP [23] and TaAs [24–26]. Besides their chiral charge, such WPs are also characterized by their Euler class invariant [17]. A non-trivial value of the Euler class prevents pairwise annihilation of colliding WPs with the same chirality inside the symmetric plane.

We consider minimal $C_{2z}\mathcal{T}$ -symmetric $\mathbf{k} \cdot \mathbf{p}$ models that describe a pair of colliding WPs with opposite chirality with trivial vs. non-trivial Euler class. For the trivial case, we consider

$$\mathcal{H}_C(\mathbf{k}) = 2(\alpha k_x k_y - m)\sigma_x + \hbar v(k_z \sigma_y + (k_x - k_y)\sigma_z), \quad (9)$$

which for $m/\alpha > 0$ exhibits a pair of WPs of opposite chirality

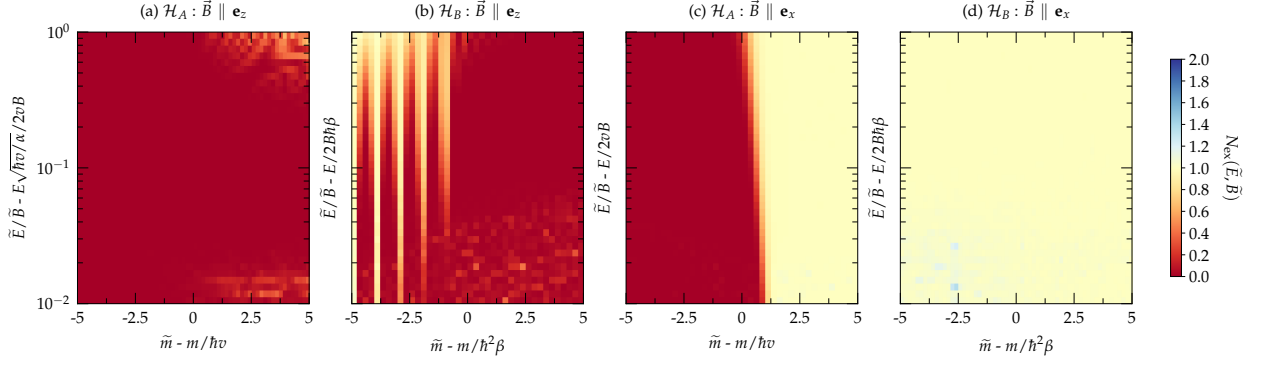


FIG. 3. Panels (a) - (d) - The expectation value $N_{\text{ex}}(\tilde{E}, \tilde{B})$ of number of electrons in the conductive bands as a function of the ratio of rescaled magnetic and electric fields - \tilde{E}/\tilde{B} and the rescaled parameter $m - \tilde{m}$ for the various orientations of magnetic field. In each of two bands 7 LLs were considered, leading to overall 13 LLs (after removing a ghost state). Slater determinants with up to $M = 2$ excited electrons (implying overall 469 Slater determinants) were used. 1402 k -points were used in the simulation of real-time dynamics. Note that for the proper identification of ghost states, the matrix representations of $\mathcal{H}_A(\mathbf{k})$ and $\mathcal{H}_B(\mathbf{k})$ are truncated at a much higher number (80) than just the number of considered LLs (13).

at $\pm(\sqrt{m/\alpha}, \sqrt{m/\alpha}, 0)$ that annihilate for $m = 0$ at $\mathbf{k} = \mathbf{0}$. We contrast this to a model with a non-trivial value of the Euler class, namely

$$\mathcal{H}_D(\mathbf{k}) = 2(\alpha k_x k_y - m)\sigma_x + \beta k_x k_z \sigma_y + \gamma(k_x^2 - k_y^2 - k_z^2)\sigma_z, \quad (10)$$

which [similar to $\mathcal{H}_C(\mathbf{k})$] for $m/\alpha > 0$ exhibits a pair of WPs of opposite chirality at $\pm(\sqrt{m/\alpha}, \sqrt{m/\alpha}, 0)$, that [as opposed to $\mathcal{H}_C(\mathbf{k})$] collide at $\mathbf{k} = \mathbf{0}$ and bounce to form WPs at $\pm(\sqrt{-m/\alpha}, -\sqrt{-m/\alpha}, 0)$ for $m < 0$. While we are unaware of material examples exhibiting Weyl points that scatter after collision due to non-trivial of the Euler class, they could potentially be implemented and probed in cold-atom setups [27].

LLs of the models are presented in Figs. 4 and 5. In the numerical calculation we set the values of $\hbar v = \alpha = 1$ for $\mathcal{H}_C(\mathbf{k})$ and $\alpha = \beta = \gamma = 1$ for $\mathcal{H}_D(\mathbf{k})$.

B. Pumping rate

In Fig. 6 we show the expectation value of excited electrons in the conductive bands - $N_{\text{ex}}(\tilde{E}, \tilde{B})$ - modifying the inter-band contribution to conductivity due to the presence of chiral anomaly for models of trivial ($\mathcal{H}_C(\mathbf{k})$) and nontrivial ($\mathcal{H}_D(\mathbf{k})$) Euler class.

The models can be easily distinguished by the application of the magnetic field along any direction. In the magnetic field applied along the z-axis, the nontrivial model ($\mathcal{H}_D(\mathbf{k})$) does not show any deviation from the value $N_{\text{ex}}(\tilde{E}, \tilde{B}) = 1$ while the trivial one ($\mathcal{H}_C(\mathbf{k})$) differs in respect to the sign of \tilde{m} . This behavior can be easily explained via the corresponding LLs.

For the trivial model, the deviation from the value $N_{\text{ex}}(\tilde{E}, \tilde{B}) = 1$ is caused by the gap opening (annihilation of

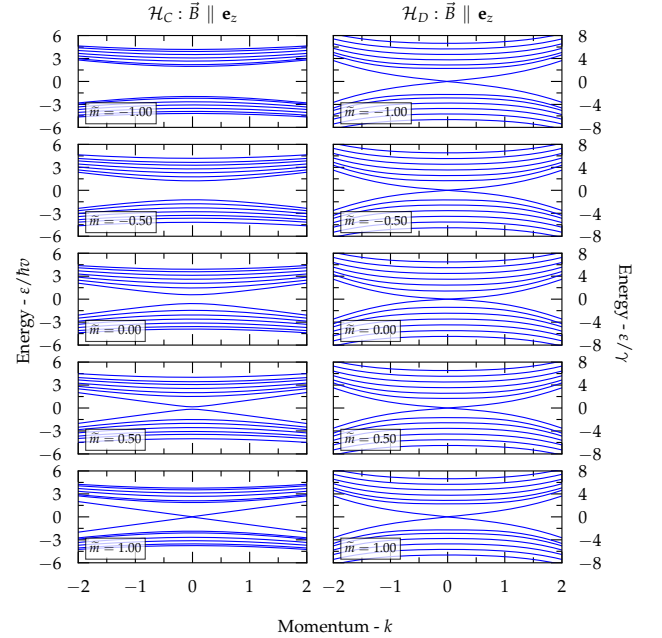


FIG. 4. LLs of $\mathcal{H}_C(\mathbf{k})$ and $\mathcal{H}_D(\mathbf{k})$ for the magnetic field oriented along the z-axis and $B = 0.5$ for various choices of \tilde{m} ($\tilde{m} = m/\hbar v$ for $\mathcal{H}_C(\mathbf{k})$ and $\tilde{m} = m/\gamma$ for $\mathcal{H}_D(\mathbf{k})$). Seven LLs below and above the Fermi level are shown.

WP), see Fig. 4, as one decreases \tilde{m} . On the contrary for non-trivial model the WP is presented for any value of \tilde{m} , see Fig. 4.

Namely, observe that the pumping rate for the Hamilto-

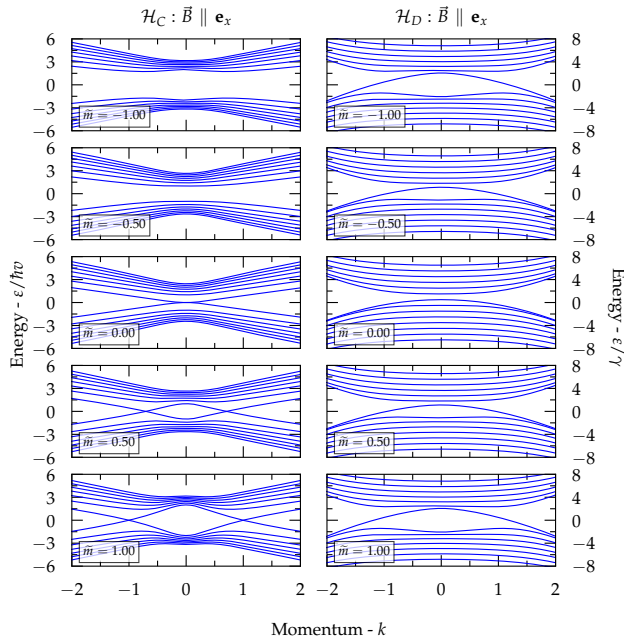


FIG. 5. LLs of $\mathcal{H}_C(\mathbf{k})$ and $\mathcal{H}_D(\mathbf{k})$ for the magnetic field oriented along the x-axis and $B = 0.5$ for various choices of \tilde{m} ($\tilde{m} = m/\hbar v$ for $\mathcal{H}_C(\mathbf{k})$ and $\tilde{m} = m/\gamma$ for $\mathcal{H}_D(\mathbf{k})$). Seven LLs below and above the Fermi level are shown.

nian $\mathcal{H}_C(\mathbf{k})$ with trivial Euler class the hybridization of chiral LLs upon the change of parameter \tilde{m} is pronounced for small values of \tilde{E}/\tilde{B} (or E/B respectively; i.e., weak electric field, strong magnetic field) *before* the Weyl points annihilate. Therefore, the decline of $N_{\text{ex}}(\tilde{E}, \tilde{B})$ from the expected limit - 1 (in here chosen units) suggests trivial class.

More interestingly, the models show nontrivial behavior when the field is applied along the x-direction. The spectrum of the nontrivial model ($\mathcal{H}_D(\mathbf{k})$) is symmetric with respect to the \tilde{m} , see Fig. 5, which manifests itself in the $N_{\text{ex}}(\tilde{E}, \tilde{B})$ as the function of \tilde{m} , see Fig. 6(d)). Note that the cusp visible at Fig. 6(d) disappears for the ratio $\tilde{E}/\tilde{B} > 1$, if one overcomes the critical value of \tilde{E} which enables tunneling also for \tilde{m} . The phase diagram of $N_{\text{ex}}(\tilde{E}, \tilde{B})$ for $\mathcal{H}_C(\mathbf{k})$, see Fig. 6(c), reveals a nontrivial structure - oscillations of $N_{\text{ex}}(\tilde{E}, \tilde{B})$ in respect to \tilde{m} which are caused by interference. The precise value of \tilde{m} for such constructive/destructive interference to happen is determined by the time the electron in the top-most valence band spends in a vicinity of the conduction bands, see LLs in Fig. 5.

V. NON-SYMMORPHIC NODAL LOOPS

A. Model

In this section, we revisit the chiral Landau levels of nodal loops protected on the boundary of the Brillouin zone by a glide symmetry [13]. The elementary model of a non-

symmorphic nodal loop (NSNL) is

$$\mathcal{H}_{\text{NSNL}}(\mathbf{k}) = \hbar v (k_x \Gamma_1 + k_y \Gamma_2 + k_z \Gamma_3) + w \Gamma_{34} \quad (11)$$

where $\{\Gamma_i\}_{i=1}^5$ are pairwise anticommuting Dirac matrices squaring to $+\mathbf{1}$, and $\Gamma_{ij} = -\frac{i}{2}[\Gamma_i, \Gamma_j]$. NSNLs can be obtained from a parent Dirac node in a \mathcal{PT} -symmetric crystal with screw rotation symmetry [28, 29] upon breaking the inversion symmetry. It has been argued by the original theoretical work on these systems [13] that NSNL exhibit Landau level crossing at zero energy for magnetic fields \mathbf{B} applied within the glide plane. Nevertheless, the chiral Landau levels are gapped if \mathbf{B} deviates from the high-symmetry plane. It has therefore been suggested that these models should exhibit a direction-selective chiral anomaly [13].

Here we use the method presented in Sec. II to investigate the disappearance of the chiral-anomalous pumping rate of the Hamiltonian in Eq. (11).

In Fig. 7 we show the band gap in LLs for $\mathbf{k} = 0$ as a function of applied magnetic field and the angle θ between the direction of the applied magnetic field and the plane of NSNL in k -space. LLs of the model as a function of the angle θ between the direction of the applied magnetic field and the plane of NSNL in k -space are presented in App. E in Figs. 11 - 13.

B. Pumping rate

In Fig. 8 we show the expectation value $N_{\text{ex}}(\tilde{E}, \tilde{B})$ as a function of the \tilde{E}, \tilde{B} and the angle θ between the direction of the applied magnetic field and the plane of NSNL in k -space. The expected $N_{\text{ex}}(\tilde{E}, \tilde{B})$ for smaller values of \tilde{E} are presented in Fig. 9.

Results shows that $N_{\text{ex}}(\tilde{E}, \tilde{B})$ is highly sensitive to the direction of the applied magnetic field θ and pronounced for small values of \tilde{E} and \tilde{B} (i.e., weak electric and magnetic fields). The *ladder of gap closing*, see Fig. 7, manifests in $N_{\text{ex}}(\tilde{E}, \tilde{B})$, see Fig. 9.

At $\theta = 90^\circ$ (the direction of the applied magnetic fields is perpendicular to the NSNL) the gap closes at $\tilde{B} = 1/n$ (in chosen units), for $n \in \mathbb{N}$. For $\theta < 90^\circ$ this *ladder of gap closing* is shifted towards weaker magnetic fields, see Fig. 7 and is observable only with sufficiently weak electric fields too, see Fig. 9.

In the limit $\theta \rightarrow 0$, the *ladder structure* is completely suppressed by the presence of NSNL, see LLs in Fig. 11 in App. E and Fig. 7. In $N_{\text{ex}}(\tilde{E}, \tilde{B})$, the value 1 is exactly recovered (which is changed only to higher values upon application of stronger electric fields). The critical value of electric field \tilde{E} to which this *ladder of gap closing* is observable is strongly dependent on θ too, see Fig. 9.

For sufficiently low value of magnetic field \tilde{B} the gap is small and the NL is present, see spectra in App. E. The length of the NSNL in the k -space is proportional to $\cos(\theta)$, where θ is the angle between the direction of the applied magnetic

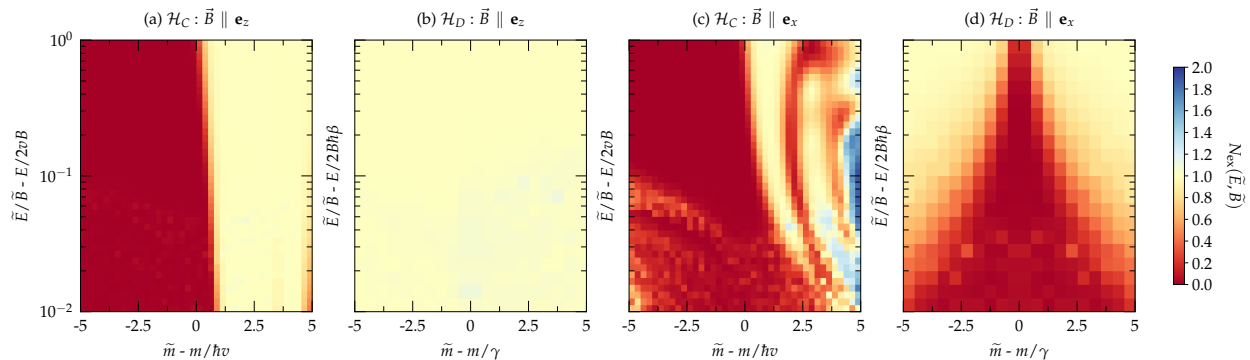


FIG. 6. The expectation value $N_{\text{ex}}(\tilde{E}, \tilde{B})$ of number of electrons in conductive bands as a function of the ratio of rescaled magnetic and electric field $-\tilde{E}/\tilde{B}$ and the rescaled parameter $m - \tilde{m}$ for various orientations of magnetic field (a) - (d). The simulation parameters were the same as for the production of Fig. 3.

VI. CONCLUSION

We demonstrated a simple numerical algorithm which allows for systematic inclusion of non-adiabatic contributions to the chiral anomaly channel of conductivity. Considering Landau-Zener-like problems and non-interacting many-body $\mathbf{k} \cdot \mathbf{p}$ models, we showed that in this conductivity channel the *relative homotopy invariant* [16] and *Euler class invariant* [17] of Weyl models manifest itself in the non-adiabatic contribution to this channel. Furthermore, for *non-symmorphic systems* [13] we showed this contribution to be highly sensitive to the direction of the applied magnetic field. Our results, upon the consideration of the other nonlinear intraband and interband contributions to the conductivity of a realistic material, can be used in the modeling of the conductivity of topological materials via the semiclassical Boltzmann transport theory as higher-order corrections. It is possible that this contribution is measurable in longitudinal magnetoresistance, if it is not suppressed by other channels of conductivity in a particular realisation in material. The presented approach can be easily applied to other $\mathbf{k} \cdot \mathbf{p}$ (e.g., double Dirac semimetals [30]) or tight-binding models.

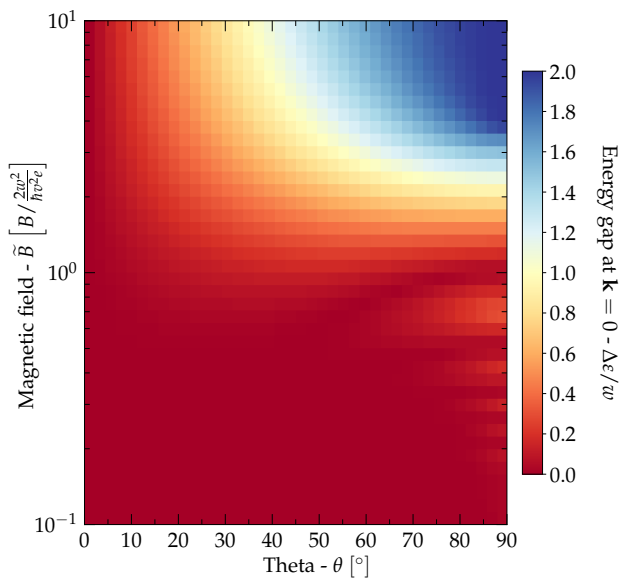


FIG. 7. Energy gap $-\Delta\epsilon/w$ of $\mathcal{H}_{\text{NSNL}}(\mathbf{k})$ at $\mathbf{k} = 0$ as a function of the magnitude of the applied magnetic field \tilde{B} and the angle θ between the direction of the applied magnetic field and NSNL. Note the *ladder of gap closing* at $\theta = 90^\circ$ and $\tilde{B} = 1/n$ for $n \in \mathbb{N}$; which manifests in $N_{\text{ex}}(\tilde{E}, \tilde{B})$, see also Fig. 9.

field and the glide plane. The length of NL affects the maximal values of \tilde{E} , see Fig. 9, where the non-trivial behavior is observable.

ACKNOWLEDGMENTS

M.B. acknowledges stimulating discussions with T. Bzdušek and A. Soluyanov. M.B. was supported by Comenius University under Grant for Young Researchers No. UK/436/2021 and by SAIA under National Scholarship Programme of the Slovak Republic in 2018. Calculations were performed on SISSA Ulysses and ETH Euler clusters.

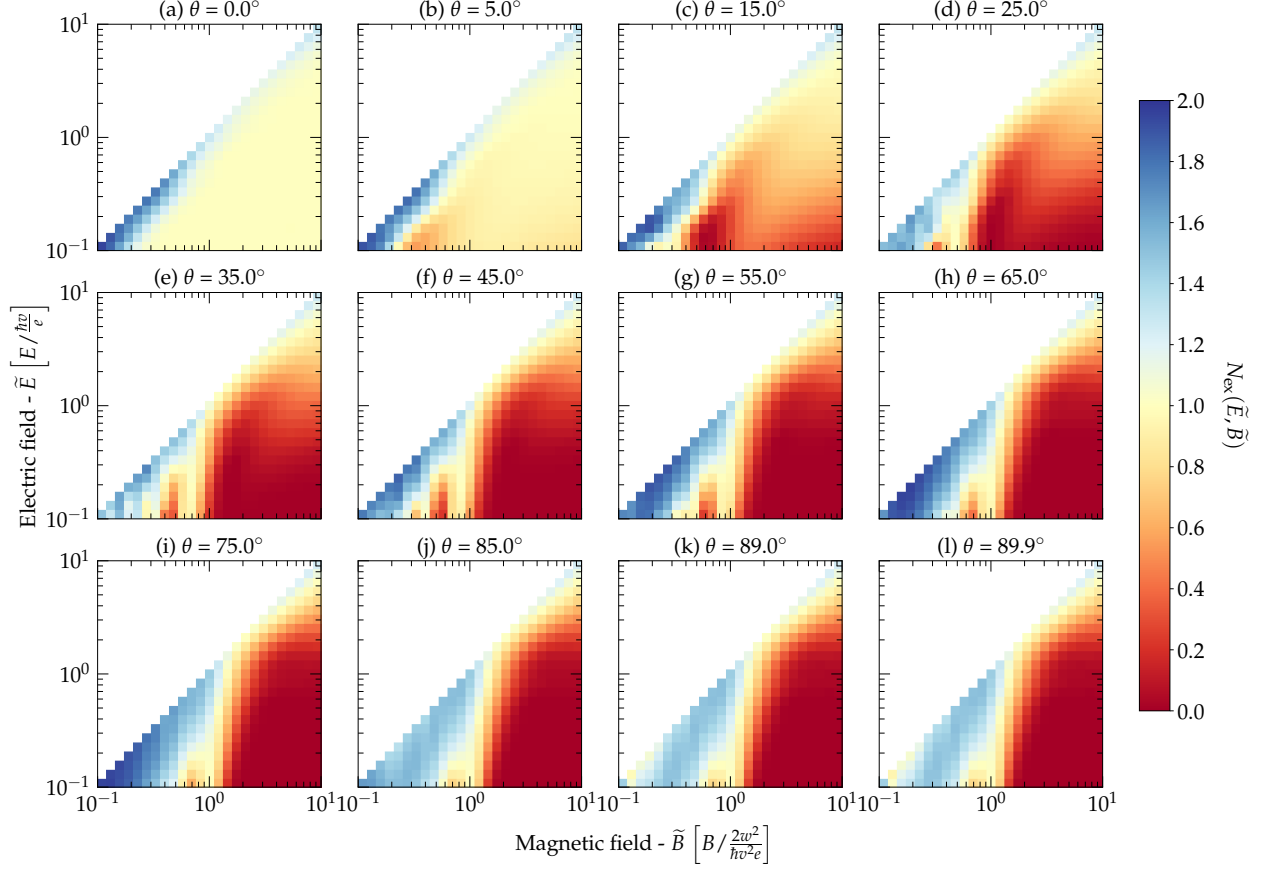


FIG. 8. The expectation value $N_{\text{ex}}(\tilde{E}, \tilde{B})$ of number of electrons in the conductive bands as a function of rescaled magnetic and electric fields - \tilde{B} and \tilde{E} . Panels (a) - (l) show disappearance of chiral-anomalous pumping if the direction of magnetic field deviates from the plane of NSNL in the region $\tilde{B} > 1$. In Fig. 9, we present details of phase diagrams for $\tilde{B} < 1$. In each of four bands of $\mathcal{H}_{\text{NSNL}}$ 5 LLs were considered, leading to $N = 9$ (after removing two ghost states). Slater determinants with up to $M = 2$ excited electrons (implying overall 1378 Slater determinants). 270 k -points were used in the simulation of real-time dynamics. The region approaching di-adiabatic limit ($\tilde{E} > \tilde{B}$) was omitted since it cannot be studied reasonably with this value of M . Note that for the proper identification of ghost states, the matrix representation of $\mathcal{H}_{\text{NSNL}}$ is truncated at a much higher number (160) than just the number of considered LLs (18).

Appendix A: Details of method

The key point of our numerical method is the observation that under the assumption of non-interacting electrons, the time evolution of many-body state $|\psi(k_z)\rangle$ can be expressed using the time evolution of single-electron states of $\mathcal{H}(k_z)$ only.

Since any choice of $\mathbf{k} \cdot \mathbf{p}$ model under presence of magnetic field implies infinitely many LL above and below the Fermi level we limit ourselves to only N above and below it. The fermionic subspace of $\mathcal{H}^{\text{many}}$ has still the dimensionality of $S = \binom{2N}{N} > 2^N$, and a naive evaluation of $\mathcal{H}^{\text{many}}$ would require $\mathcal{O}(N^N)$ time. To avoid this, we express the many-electron wave function $|\psi(k_z)\rangle$ in the basis of a limited number of Slater determinants created from the single-electron wave functions $|\psi_n(k_z)\rangle$. We limit only to the Slater determinants containing

up to M ($M < N$) electrons in the excited ($\varepsilon_n > 0$) single-particle states. That creates a basis of $S_M = \sum_{i=0}^M \binom{N}{i}^2 \sim N^M$ Slater determinants $|\varphi_i(k_z)\rangle$.

The many-electron wave function $|\psi(k_z)\rangle$ can then be expressed as

$$|\psi(k_z)\rangle = \sum_i^{S_M} c_i(k_z) |\varphi_i(k_z)\rangle, \quad (\text{A1})$$

where $|\varphi_i(k_z)\rangle$ is a Slater determinant of the form

$$|\varphi_i(k_z)\rangle = \frac{1}{\sqrt{N!}} \sum_{\tau} \text{sign } \tau \left(\otimes_j |\psi_{\tau(\alpha_i(j))}(k_z)\rangle \right), \quad (\text{A2})$$

in which $\text{sign } \tau = \pm 1$ is the parity of permutation τ and $\alpha_i(j)$ goes over the set of N one-electron states from which the Slater determinant is constructed.

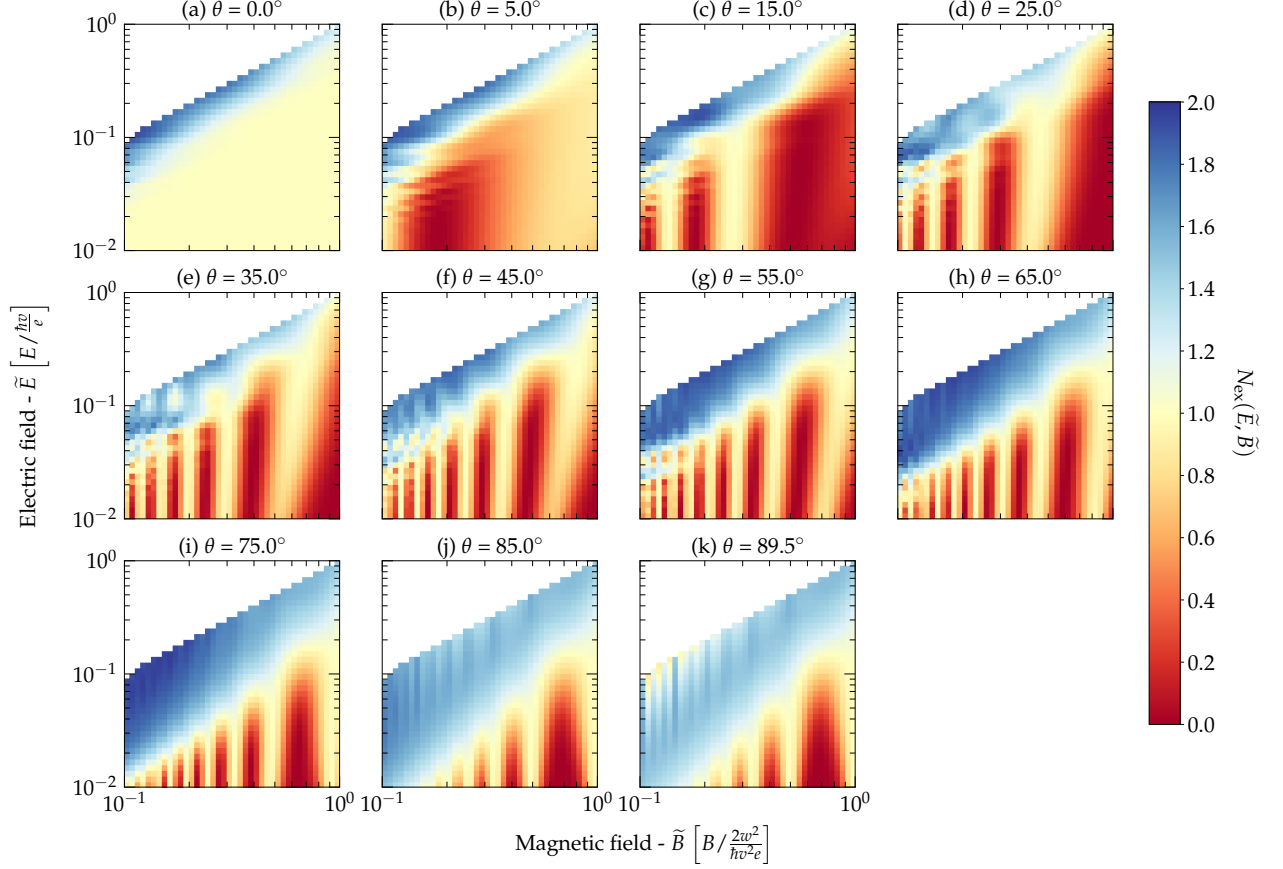


FIG. 9. The expectation $N_{\text{ex}}(\tilde{E}, \tilde{B})$ of number of electrons in the conductive bands as a function of rescaled magnetic and electric fields - \tilde{B} and \tilde{E} in the region $\tilde{B} < 1$. All parameters of simulations are the same as for the phase diagrams presented in Fig. 8. Panels (a) - (b) show disappearance of chiral-anomalous pumping if the direction of magnetic field without any additional structure. Panels (c) - (k) reveal additional structures on disappearance of anomalous-chiral anomaly due to gap closing of $\mathcal{H}_{\text{NSNL}}$ at certain values of magnetic field. Note that this "ladder" structure shifts towards smaller \tilde{B} with increasing the deviation (θ) of applied magnetic field from the NSNL plane.

Under the assumption of non-interacting electrons, the Slater determinant $|\varphi_i(k_z)\rangle$ is an eigenstate of $\mathcal{H}^{\text{many}}(k_z)$ with energy $\varepsilon_i(k_z) = \sum_{j=1}^N \varepsilon_{\alpha(j)}(k_z)$. Thus, it follows that the many-electron TDSE (Eq. (4)) (almost) diagonalizes in Slater formalism into the simple system of dimensionality S_M ,

$$i\hbar C_{ij}^{-1} \partial_t c_j(k_z) = \varepsilon_i(k_z) c_i(k_z), \quad (\text{A3})$$

where C_{ij} is the overlap matrix between the eigenstates of $\mathcal{H}^{\text{many}}(k_z + \Delta k)$ and the eigenstates of $\mathcal{H}^{\text{many}}(k_z)$.

The solution of Eq. (A3) just requires to find a suitable time propagator $\mathcal{U}_{ij}(t + \Delta t, t)$ which under Eq. (3) can be written as $\mathcal{U}_{ij}(k_z - \Delta k, k_z)$.

The time evolution can than be expressed only as a problem of evolution of basis set coefficients and a simple matrix-vector equation given a suitable propagator $\mathcal{U}_{ij}(k_z - \Delta k, k_z)$ exists,

$$c_i(k_z - \Delta k) = \mathcal{U}_{ij}(k_z - \Delta k, k_z) c_j(k_z). \quad (\text{A4})$$

We choose a simple Euler forward propagator

$$\begin{aligned} \mathcal{U}_{ij}(k_z - \Delta k, k_z) = & \sum_{n=0}^{S_M} \langle \varphi_i(k_z - \Delta k) | \varphi_n(k_z - \Delta k/2) \rangle \cdot \\ & \exp\left(\frac{i\Delta k_z}{E} \varepsilon_n(k_z - \Delta k/2)\right) \cdot \\ & \langle \varphi_n(k_z - \Delta k/2) | \varphi_j(k_z) \rangle. \end{aligned} \quad (\text{A5})$$

and achieve the unitarity of the time evolution by the normalisation of the wave function after every step. Note that we do not choose an implicit propagator, since that would bring an additional factor of $\mathcal{O}(S_M)$ to the overall complexity of the method. Rather, we achieve the numerical stability using a small step Δk .

Since the dot product of two Slater determinants can be calculated in $\mathcal{O}(N^3)$ steps, see App. D, the whole evolution can be evaluated in $\mathcal{O}(S_M^2 N^3) \sim \mathcal{O}(N^{2M+3})$ steps.

The demonstration of our method for the case of the isotropic Weyl point $\mathbf{k} \cdot \mathbf{p}$ model is presented in App. B.

Appendix B: Demonstration of the method on the isotropic Weyl point model

To demonstrate our method, we apply it one (isotropic) WP model adapted from Ref. [5]. We consider the ideal Weyl Hamiltonian as

$$\mathcal{H} = \hbar v \mathbf{k} \cdot \boldsymbol{\sigma}, \quad (\text{B1})$$

where $\boldsymbol{\sigma} = (\sigma_x, \sigma_y, \sigma_z)$ are standard anticommuting 2×2 Pauli matrices, v has dimension of velocity, and \mathbf{k} is the momentum. The energy spectrum of this Hamiltonian is $\varepsilon_{\pm}(\mathbf{k}) = \pm \hbar v k$. Considering the ideal Weyl Hamiltonian in parallel magnetic and electric fields we can model the presence of a magnetic field by performing the Peierls substitution. We assume electric and magnetic fields to be

$$\mathbf{B} = (0, 0, B) \quad \text{and} \quad \mathbf{E} = (0, 0, E). \quad (\text{B2})$$

The Peierls substitution changes the operators of momentum,

$$\begin{aligned} (\hbar k_x, \hbar k_y, \hbar k_z) &\mapsto (-i\hbar\partial_x + eA_x, -i\hbar\partial_y + eA_y, \hbar k_z) \\ &\equiv (\Pi_x, \Pi_y, \hbar k_z), \end{aligned} \quad (\text{B3})$$

and the canonical momentum commutator changes to

$$[\Pi_x, \Pi_y] = ie\hbar(\partial_y A_x - \partial_x A_y) = -ie\hbar B. \quad (\text{B4})$$

Hence, the Π -operators can be expressed using the usual ladder operators $[a, a^\dagger] = 1$ as

$$\begin{aligned} \Pi_x &= \sqrt{\frac{e\hbar|B|}{2}}(a + a^\dagger) \\ \Pi_y &= i\text{sign}(B)\sqrt{\frac{e\hbar|B|}{2}}(a - a^\dagger). \end{aligned} \quad (\text{B5})$$

Assuming $B > 0$, the ideal Weyl Hamiltonian is changed into

$$\mathcal{H}(k_z) = v \begin{pmatrix} \hbar k_z & \sqrt{2e\hbar B}a \\ \sqrt{2e\hbar B}a^\dagger & -\hbar k_z \end{pmatrix}. \quad (\text{B6})$$

The corresponding energy spectrum is

$$\begin{aligned} \varepsilon_0(k_z) &= -v\hbar k_z \\ \forall n \in \mathbb{Z} \setminus \{0\} : \varepsilon_n(k_z) &= \text{sign}(n)v\sqrt{\hbar^2 k_z^2 + 2e\hbar B|n|}. \end{aligned} \quad (\text{B7})$$

We define rescaled fluxes of electric and magnetic fields and expressed energy in multiples of $\hbar v$,

$$\tilde{E} = eE/\hbar v, \quad \tilde{B} = 2eB/\hbar, \quad \text{and} \quad \tilde{\varepsilon} = \varepsilon/(\hbar v). \quad (\text{B8})$$

In this convention, $\mathcal{H}(k_z)$ takes the form

$$\tilde{\mathcal{H}}(k_z) = \begin{pmatrix} k_z & \sqrt{\tilde{B}}a \\ \sqrt{\tilde{B}}a^\dagger & -k_z \end{pmatrix}, \quad (\text{B9})$$

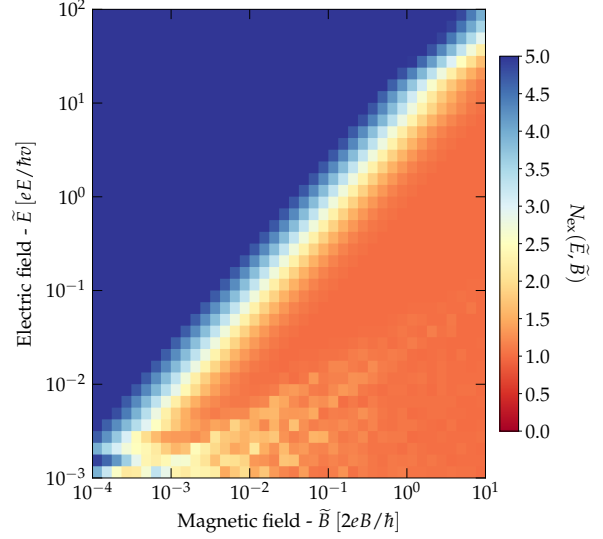


FIG. 10. The expectation value $N_{\text{ex}}(\tilde{E}, \tilde{B})$ of number of electrons in the conductive bands as a function of rescaled magnetic and electric fields $-\tilde{B}$ and \tilde{E} for ideal Weyl Hamiltonian given by Eq. (B1). Overall 13 LLs (after removal of one ghost state) were considered ($N = 7$), with up to $M = 5$ excited electrons yielding to overall 1709 Slater determinants. 283 k -points were used for the real-time dynamics simulation.

and the TDSE takes form

$$i\partial_{k_z} |\psi(k_z)\rangle = -1/\tilde{E}\tilde{\mathcal{H}}(k_z) |\psi(k_z)\rangle. \quad (\text{B10})$$

Results of our method for this simple model are presented in Fig. 10. The diagram shows that for the Hamiltonian given by Eq. (B1) the expectation value of $N_{\text{ex}}(\tilde{E}, \tilde{B})$ depends on \tilde{B} and \tilde{E} only via their ratio $-\tilde{E}/\tilde{B}$ as heuristically argued in App. C. Note also a numerical noise visible in Fig. 10 in $N_{\text{ex}}(\tilde{E}, \tilde{B})$ in the region with $\tilde{E} < 10^{-2}$ where the used step Δk becomes inappropriate. The value of Δk were kept constant in all calculations presented in the phase diagram.

Appendix C: Heuristic argument for the dependence on the ratio $-\tilde{B}/\tilde{E}$ only in isotropic WSM

The single-electron TDSE given in Eq. (B10) can be formally mapped to the class of Hamiltonians studied by Brundobler and Elser [31] (to the generalization of Landau-Zener problem). The corresponding TDSE in their notation becomes

$$\begin{aligned} \mathcal{H}(t) &= \mathcal{A} + \mathcal{B}t, \\ i\partial_t \psi(t) &= \mathcal{H}(t)\psi(t), \end{aligned} \quad (\text{C1})$$

where \mathcal{A} and \mathcal{B} are constant Hermitian matrices. The identification is done as follows,

$$\begin{aligned} t &\rightarrow k_z, \\ \mathcal{A} &\rightarrow \begin{pmatrix} 0 & -\sqrt{\tilde{B}/\tilde{E}\alpha} \\ -\sqrt{\tilde{B}/\tilde{E}\alpha^\dagger} & 0 \end{pmatrix}, \\ \mathcal{B} &\rightarrow \begin{pmatrix} -1/\tilde{E} & 0 \\ 0 & 1/\tilde{E} \end{pmatrix}. \end{aligned} \quad (\text{C2})$$

Brundobler and Elser [31] found that elements of S-matrix for the time evolution given by Eq. (C1) can be approximated and expressed in terms of the transition probabilities p_{kl} between the two states (of $\mathcal{H}(t)$ k and l only),

$$p_{kl} \approx e^{-\pi z_{kl}}, \quad (\text{C3})$$

where z_{kl} is the Landau-Zener parameter

$$z_{kl} = \frac{|\mathcal{A}_{kl}|^2}{|\mathcal{B}_{kk} - \mathcal{B}_{ll}|} \sim \tilde{B}/\tilde{E}. \quad (\text{C4})$$

Even though, we do not study the Landau-Zener problem of a single-electron Hamiltonian $\mathcal{H}(t)$, but rather a many-body Hamiltonian of its tensor product, it gives an insight, why only the ratio of electric and magnetic fields (fluxes) should influence the non-adiabatic correction to the chiral anomaly for isotropic WP as demonstrated in Fig. 10.

Appendix D: Calculation of dot product of two Slater determinants in $O(N^3)$

Here we show how the dot product of two Slater determinants can be calculated in $O(N^3)$ time. Considering two Slater determinants

$$|\varphi_i\rangle = \frac{1}{\sqrt{N!}} \sum_{\tau} \text{sign } \tau \left(\otimes_k |\psi_{\tau(\alpha_i(k))}\rangle \right) \quad (\text{D1})$$

$$|\varphi'_j\rangle = \frac{1}{\sqrt{N!}} \sum_{\tau'} \text{sign } \tau' \left(\otimes_l |\psi'_{\tau'(\alpha_j(l))}\rangle \right), \quad (\text{D2})$$

we are interested into their dot product

$$\langle \varphi_i | \varphi'_j \rangle = \frac{1}{N!} \sum_{\tau'} \sum_{\tau} \text{sign } \tau' \text{sign } \tau \left(\prod_{k=1}^N \langle \psi_{i\tau(k)} | \psi'_{j\tau'(k)} \rangle \right). \quad (\text{D3})$$

Note that although the direct evaluation of the dot product requires $(N!)^2$ operations, there are just N^2 independent terms. Note also that the determinant of the matrix $M_{ij} = \langle \psi_i | \psi'_j \rangle$ can be expressed as

$$\det M \equiv \sum_{\tau'} \text{sign } \tau' \prod_{i=1}^N \langle \psi_i | \psi'_{\tau'(i)} \rangle, \quad (\text{D4})$$

where τ' is the corresponding permutation. Using $\det(AB) = \det A \cdot \det B$, one can see that matrix M permuted by τ has a determinant $\det(\tau M)$ equal to $\text{sign } \tau \det M$. On the other hand, $(\tau M)_{ij} = \langle \psi_{\tau(i)} | \psi'_j \rangle$, and thus it follows that

$$\begin{aligned} \det(\tau M) &\equiv \sum_{\tau'} \text{sign } \tau' \prod_{i=1}^N \langle \psi_{\tau(i)} | \psi'_{\tau'(i)} \rangle \\ &= \text{sign } \tau \det M. \end{aligned} \quad (\text{D5})$$

By multiplying both sides of the last equation by $\text{sign } \tau$ and summing over all $N!$ permutations covered by τ , we identify in $\det M$ the dot product of two Slater determinants $\langle \varphi_i | \varphi'_j \rangle$,

$$\langle \varphi_i | \varphi'_j \rangle = \det M. \quad (\text{D6})$$

We note that this formula was for the first time presented in Ref. [32].

Appendix E: Landau Levels of model non-symmorphic nodal loop Hamiltonian

In Figs. 11 - 13 we show the LLs of the model NSNL Hamiltonian - $\mathcal{H}_{\text{NSNL}}$ given by Eq. (11) as a function of the angle θ between the direction of the applied magnetic field and the plane of NSNL in the reciprocal space.

-
- [1] N. P. Armitage, E. J. Mele, and A. Vishwanath, Weyl and dirac semimetals in three-dimensional solids, *Rev. Mod. Phys.* **90**, 015001 (2018).
 - [2] B. Yan and C. Felser, Topological materials: Weyl semimetals, *Annual Review of Condensed Matter Physics* **8**, 337 (2017).
 - [3] X. Wan, A. M. Turner, A. Vishwanath, and S. Y. Savrasov, Topological semimetal and fermi-arc surface states in the electronic structure of pyrochlore iridates, *Physical Review B* **83**, 10.1103/physrevb.83.205101 (2011).
 - [4] C. Rylands, A. Parhizkar, A. A. Burkov, and V. Galitski, Chiral anomaly in interacting condensed matter systems, *Physical Review Letters* **126**, 10.1103/physrevlett.126.185303 (2021).
 - [5] P. Hosur and X. Qi, Recent developments in transport phenomena in weyl semimetals, *Comptes Rendus Phys.* **14**, 857 (2013).
 - [6] A. A. Zyuzin and A. A. Burkov, Topological response in weyl semimetals and the chiral anomaly, *Physical Review B* **86**, 10.1103/physrevb.86.115133 (2012).
 - [7] D. T. Son and B. Z. Spivak, Chiral anomaly and classical negative magnetoresistance of weyl metals, *Phys. Rev. B* **88**, 104412 (2013).
 - [8] P. E. C. Ashby and J. P. Carbotte, Magneto-optical conductivity of weyl semimetals, *Physical Review B* **87**, 10.1103/physrevb.87.245131 (2013).
 - [9] H.-Z. Lu, S.-B. Zhang, and S.-Q. Shen, High-field magnetoconductivity of topological semimetals with short-range potential, *Physical Review B* **92**, 10.1103/physrevb.92.045203 (2015).
 - [10] C. J. Tabert, J. P. Carbotte, and E. J. Nicol, Optical and transport properties in three-dimensional dirac and weyl semimetals,

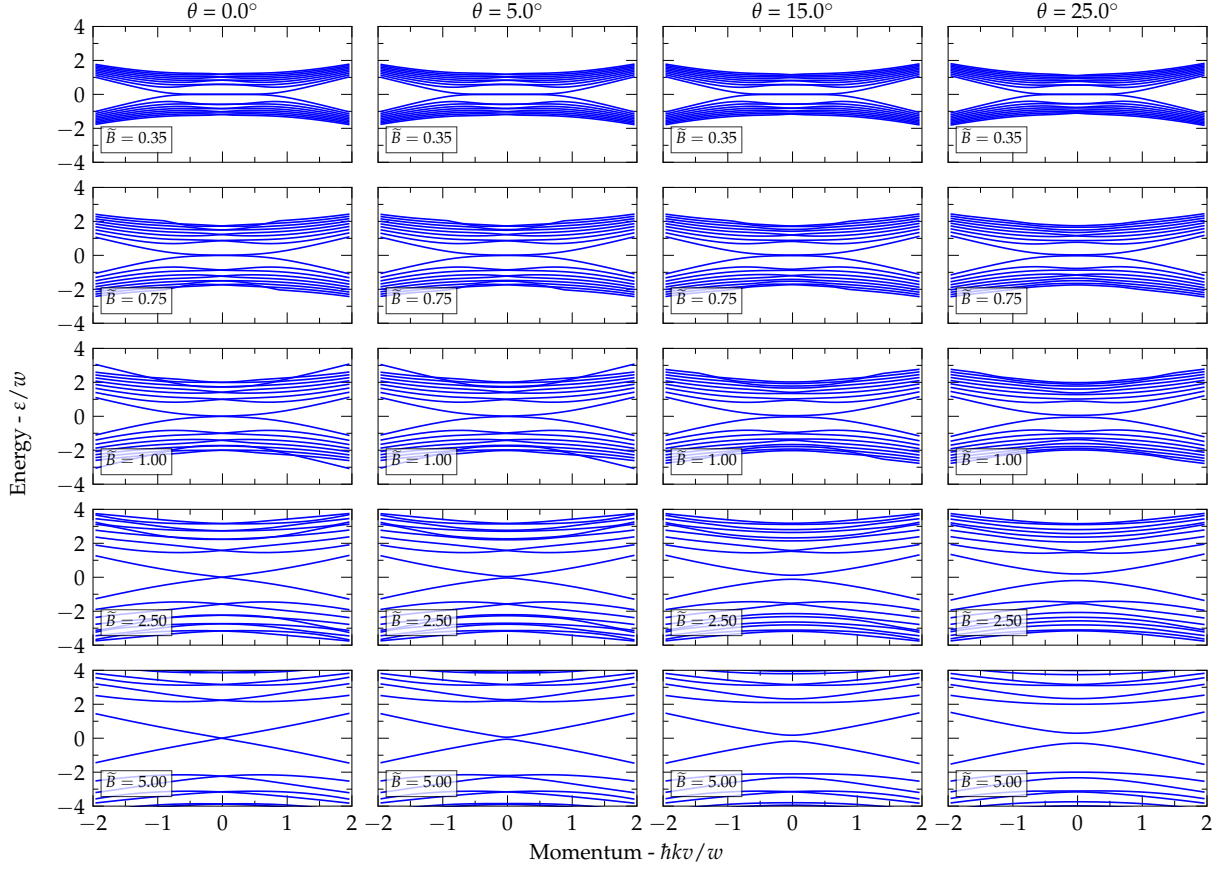


FIG. 11. LLs of $\mathcal{H}_{\text{NSNL}}$. Nine LLs below and above the Fermi level are shown.

- Physical Review B **93**, [10.1103/physrevb.93.085426](https://doi.org/10.1103/physrevb.93.085426) (2016).
- [11] C. J. Tabert and J. P. Carbotte, Optical conductivity of weyl semimetals and signatures of the gapped semimetal phase transition, Physical Review B **93**, [10.1103/physrevb.93.085442](https://doi.org/10.1103/physrevb.93.085442) (2016).
- [12] X. Dai, Z. Du, and H.-Z. Lu, Negative magnetoresistance without chiral anomaly in topological insulators, Physical Review Letters **119**, [10.1103/physrevlett.119.166601](https://doi.org/10.1103/physrevlett.119.166601) (2017).
- [13] T. Bzdušek, Q. Wu, A. Rüegg, M. Sigrist, and A. A. Soluyanov, Nodal-chain metals, *Nature* **538**, 75 (2016).
- [14] S. Zhang, Q. Wu, Y. Liu, and O. V. Yazyev, Magnetoresistance from fermi surface topology, Physical Review B **99**, [10.1103/physrevb.99.035142](https://doi.org/10.1103/physrevb.99.035142) (2019).
- [15] R.-H. Li, O. G. Heinonen, A. A. Burkov, and S. S.-L. Zhang, Nonlinear hall effect in weyl semimetals induced by chiral anomaly, Physical Review B **103**, [10.1103/physrevb.103.045105](https://doi.org/10.1103/physrevb.103.045105) (2021).
- [16] X.-Q. Sun, S.-C. Zhang, and T. Bzdušek, Conversion Rules for Weyl Points and Nodal Lines in Topological Media, *Phys. Rev. Lett.* **121**, 106402 (2018).
- [17] A. Bouhon, Q. Wu, R.-J. Slager, H. Weng, O. V. Yazyev, and T. Bzdušek, Non-abelian reciprocal braiding of weyl points and its manifestation in ZrTe, *Nature Physics* **16**, 1137 (2020).
- [18] L.-K. Lim and R. Moessner, Pseudospin Vortex Ring with a Nodal Line in Three Dimensions, *Phys. Rev. Lett.* **118**, 016401 (2017).
- [19] G. Xu, H. Weng, Z. Wang, X. Dai, and Z. Fang, Chern Semimetal and the Quantized Anomalous Hall Effect in HgCr_2Se_4 , *Phys. Rev. Lett.* **107**, 186806 (2011).
- [20] A. Nelson, T. Neupert, A. Alexandradinata, and T. Bzdušek, Delicate topology protected by rotation symmetry: Crystalline hopf insulators and beyond, [arXiv:2111.09365v1](https://arxiv.org/abs/2111.09365v1).
- [21] Q. Wu, A. A. Soluyanov, and T. Bzdušek, Non-abelian band topology in noninteracting metals, *Science* **365**, 1273 (2019).
- [22] A. A. Soluyanov, D. Gresch, Z. Wang, Q.-S. Wu, M. Troyer, X. Dai, and B. A. Bernevig, Type-II Weyl semimetals, *Nature* **527**, 495 (2015).
- [23] B. Q. Lv, Z.-L. Feng, Q.-N. Xu, X. Gao, J.-Z. Ma, L.-Y. Kong, P. Richard, Y.-B. Huang, V. N. Strocov, C. Fang, H.-M. Weng, Y.-G. Shi, T. Qian, and H. Ding, Observation of three-component fermions in the topological semimetal molybdenum phosphide, *Nature* **546**, 627 (2017).
- [24] H. Weng, C. Fang, Z. Fang, B. A. Bernevig, and X. Dai, Weyl Semimetal Phase in Noncentrosymmetric Transition-Metal Monophosphides, *Phys. Rev. X* **5**, 011029 (2015).

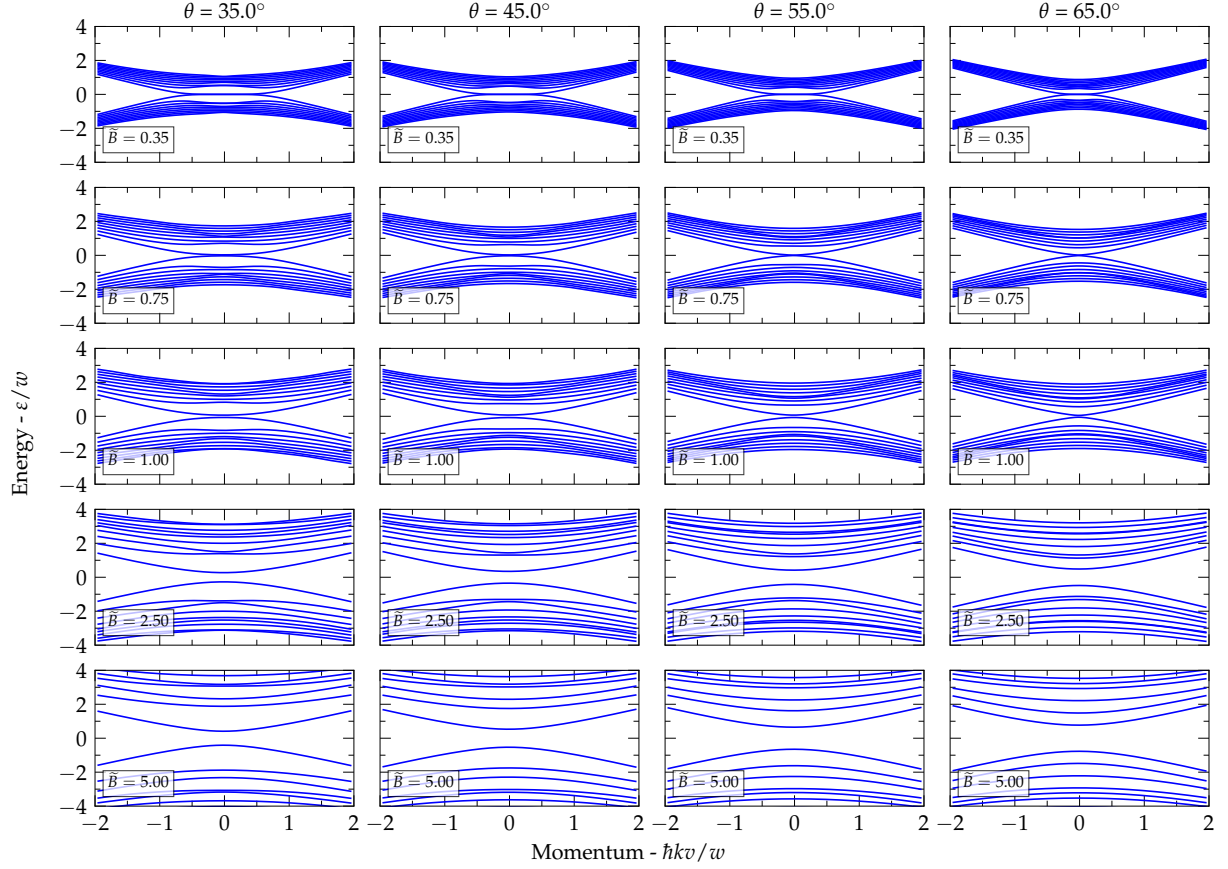


FIG. 12. LLs of $\mathcal{H}_{\text{NSNL}}$. Nine LLs below and above the Fermi level are shown.

- [25] B. Q. Lv, H. M. Weng, B. B. Fu, X. P. Wang, H. Miao, J. Ma, P. Richard, X. C. Huang, L. X. Zhao, G. F. Chen, Z. Fang, X. Dai, T. Qian, and H. Ding, Experimental Discovery of Weyl Semimetal TaAs, *Phys. Rev. X* **5**, 031013 (2015).
- [26] S.-Y. Xu, I. Belopolski, N. Alidoust, M. Neupane, G. Bian, C. Zhang, R. Sankar, G. Chang, Z. Yuan, C.-C. Lee, S.-M. Huang, H. Zheng, J. Ma, D. S. Sanchez, B. Wang, A. Bansil, F. Chou, P. P. Shibayev, H. Lin, S. Jia, and M. Z. Hasan, Discovery of a Weyl fermion semimetal and topological Fermi arcs, *Science* **349**, 613 (2015).
- [27] F. N. Ünal, A. Bouhon, and R.-J. Slager, Topological euler class as a dynamical observable in optical lattices, *Physical Review Letters* **125**, 10.1103/physrevlett.125.053601 (2020).
- [28] S. M. Young, S. Zaheer, J. C. Y. Teo, C. L. Kane, E. J. Mele, and A. M. Rappe, Dirac semimetal in Three Dimensions, *Phys. Rev. Lett.* **108**, 140405 (2012).
- [29] B.-J. Yang and N. Nagaosa, Classification of stable three-dimensional Dirac semimetals with nontrivial topology, *Nat. Commun.* **5**, 4898 (2014).
- [30] B. J. Wieder, Y. Kim, A. Rappe, and C. Kane, Double dirac semimetals in three dimensions, *Physical Review Letters* **116**, 10.1103/physrevlett.116.186402 (2016).
- [31] S. Brundobler and V. Elser, S-matrix for generalized landau-zener problem, *Journal of Physics A: Mathematical and General* **26**, 1211 (1993).
- [32] P.-O. Löwdin, Quantum theory of many-particle systems. i. physical interpretations by means of density matrices, natural spin-orbitals, and convergence problems in the method of configurational interaction, *Physical Review* **97**, 1474 (1955).

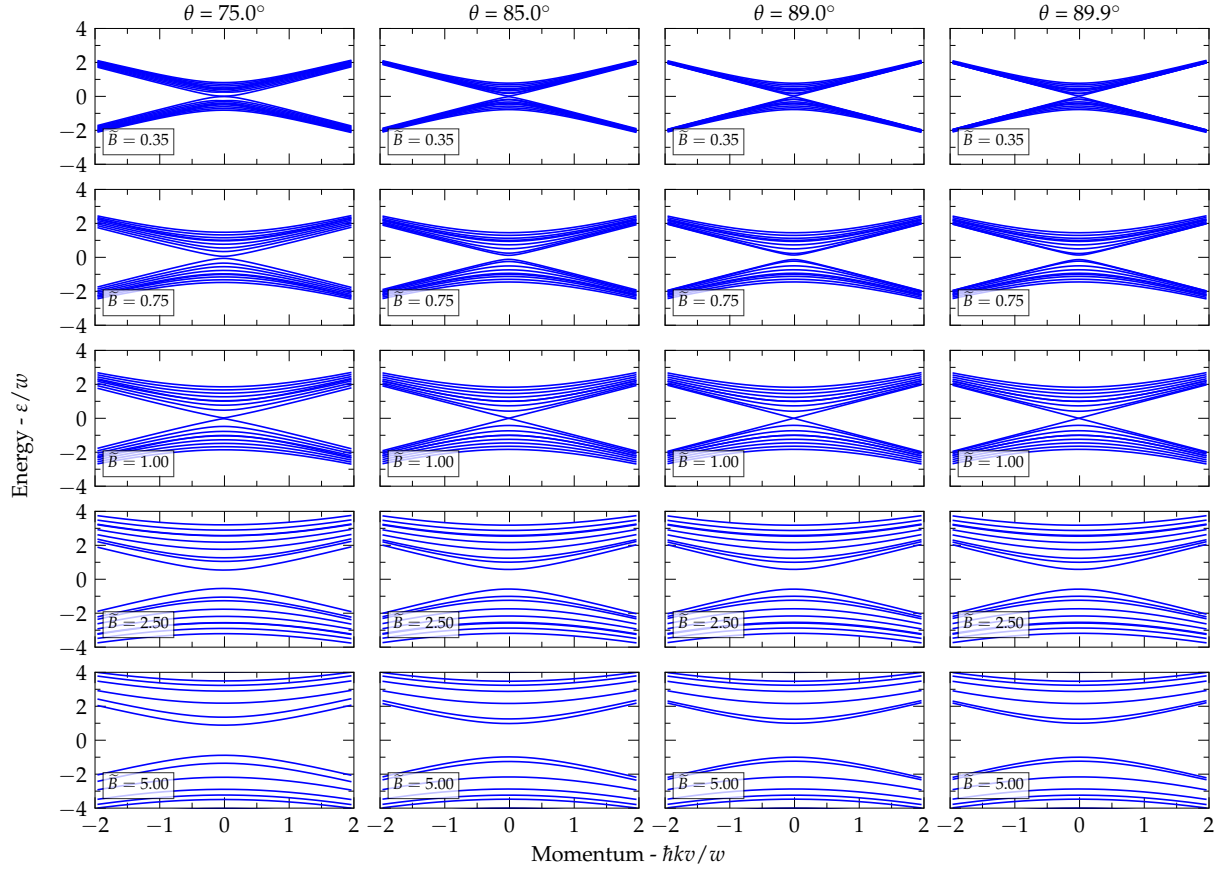


FIG. 13. LLs of $\mathcal{H}_{\text{NSNL}}$. Nine LLs below and above the Fermi level are shown.